Ground and excited states of iron centers in ZnO: Pulse-EPR and magneto-optical spectroscopy

D. V. Azamat,[1] J. Debus,[2] D. R. Yakovlev,[2,3] V. Yu. Ivanov,[4] M. Godlewski,[4,5] M. Fanciulli,[6,7] and M. Bayer[2,3]

[1]*Institute of Physics AS CR, 182 21, Prague 8, Czech Republic*
[2]*Experimentelle Physik 2, Technische Universität Dortmund, 44227 Dortmund, Germany*
[3]*Ioffe Physical-Technical Institute, Russian Academy of Sciences, 194021 St. Petersburg, Russia*
[4]*Institute of Physics, Polish Academy of Sciences, Warsaw 02-668, Poland*
[5]*Dept. Mathematics and Natural Sciences College of Science, Cardinal S. Wyszynski University, Warsaw, Poland*
[6]*Laboratorio Nazionale MDM, CNR-IMM, 20041 Agrate Brianza (MI), Italy*
[7]*Dipartimento di Scienza dei Materiali, Universita degli studi di Milano-Bicocca, Milano, Italy*

We report on the ground- and excited-state properties of Fe^{3+} centers in hydrothermally and chemical-vapor-transport grown single ZnO crystals studied by continuous-wave electron-paramagnetic resonance (EPR) under dark and laser-illuminated conditions, pulsed-EPR and magneto-photoluminescence. By use of EPR experiments, the fine-structure parameters of the Fe^{3+} spin Hamiltonian are determined. Three types of charge-compensated Fe^{3+} centers are identified and the charge conversion from Fe^{2+} to Fe^{3+} is highlighted. The magneto-optical studies of the Zeeman components of the spin-forbidden electric-dipole transitions from excited $^4T_1(G)$ to ground $^6A_1(^6S)$ states of the Fe^{3+} center indicate the trigonal symmetry of the fine structure of the lowest $\Gamma_8(^4T_1)$ excited state. The energy positions of the Zeeman components are measured in the external magnetic field of 8 T rotated in $(1\bar{2}10)$ and (0001) crystal planes. The angular variation of the Zeeman lines exhibits two magnetically nonequivalent Fe^{3+} centers. These features result from the contribution of high-rank Zeeman terms of dimension $\mathbf{B}J^3$ in the spin Hamiltonian. For the electron spin $S = 5/2$ system of the trigonal Fe^{3+} ion, we further demonstrate the tuning of one-photon Rabi oscillations by means of electron spin-echo measurements.

I. INTRODUCTION

ZnO has attracted remarkable attention as a promising material for optoelectronics and spintronics applications [1–4]; in particular, its magnetic properties, which can be controlled by doping with transition metal ions, are of interest. Despite some basic understanding, the role of dopants and native defects on the magnetic, electronic as well as optical properties of ZnO is still under discussion [5–8]. In this context, strong attention is paid to the associated Fe^{3+} impurities in ZnO. Various types of Fe^{3+} centers, which are interpreted as the substitution of Zn by Fe^{3+}, have been studied by electron-paramagnetic resonance spectroscopy [9–13]. Hereby, different kinds of iron centers can be established: besides a regular lattice environment of the Fe^{3+} center with trigonal symmetry undisturbed by a defect, there are three types of charge-compensated Fe^{3+} centers that are compensated by neighboring Li^+ ions [10]. The modifications of the Fe^{3+} center due to a neighboring Li^+ ion are still not well understood; therefore, a combination of various experimental techniques supported by theoretical calculations shall be very instructive.

Under dark conditions, the one of dominant donors in ZnO is the Fe^{2+} impurity [14,15]; however, the illumination with visible or ultraviolet light converts a portion of the Fe^{2+} to Fe^{3+} centers. The Fe^{3+} centers are responsible for the photoluminescence (PL) band at 1.78 eV assigned to iron intracenter transitions, as reported by Heitz *et al.* [16]. The aim of our study is to precisely determine the fine structure of the $^4T_1(G)$ excited Fe^{3+} state in bulk ZnO by means of magneto-optical spectroscopy. The splitting of the $^4T_1(G)$ state of Fe^{3+} in trigonal C_{3v} symmetry is evaluated from the structure of the sharp zero-phonon lines in luminescence.

Hereby, the angular dependence of the Zeeman effect allows us to identify the fine-structure components. Their splittings in a magnetic field are calculated with an effective Hamiltonian including high-rank Zeeman interaction of the form $\mathbf{B}J^3$. In addition to the magneto-optical experiments, which provide information on the excited states of the Fe^{3+} centers, EPR measurements yield information on their ground state and charge conversion.

The trigonal Fe^{3+} ion with electron spin $S = 5/2$ potentially provides a spin multiplet for use in the implementation of quantum algorithms [17–22]. Up to now, systems with the same ground-state electron configuration, like Mn^{2+} ($3d^5$) implanted in single MgO crystals or colloidal ZnO quantum dots, have been suggested for quantum computing applications [23–26]. In that context, a long electron spin coherence time has been observed for the Fe^{3+} ground state at low temperature in recent studies by use of Fourier-transform EPR [27]. Here, we report on spin-echo measurements of Fe^{3+} system (in an external magnetic field parallel to the crystalline c axis) giving insight into the decoherence mechanism of the one-photon Rabi oscillations.

The paper is organized as follows. In Sec. II, the studied samples and the experimental setups are described. EPR spectra of different Fe^{3+} centers under dark condition and optical excitation are presented in Sec. III. In Sec. IV, the one-photon Rabi oscillations for the trigonal Fe^{3+} center are discussed. In Sec. V, the magneto-optical properties of the Fe^{3+} zero-phonon lines are highlighted. The structure of the ground and excited energy levels of Fe^{3+} in C_{3v} crystal field including spin-orbit coupling is determined experimentally and theoretically by considering their angular dependent Zeeman splittings.

II. EXPERIMENTAL DETAILS

The bulk ZnO crystals were grown by the hydrothermal or chemical-vapor-transport (CVT) technique. For the magneto-optical and pulsed EPR studies, a $4 \times 4 \times 0.5$ mm^3 single crystal of hydrothermally grown ZnO was used. It was doped with iron at concentration of about 10^{20} cm^{-3}. A hydrothermally grown ZnO crystal with an iron concentration of about 10^{18} cm^{-3} was studied by continuous-wave EPR. An iron-doped CVT grown ZnO sample was also used for the magneto-optical experiments that yielded similar results compared to that for the hydrothermally grown sample.

The continuous-wave (CW) EPR measurements were performed with a Bruker Elexsys 580 spectrometer operating at X- and Q-band frequencies of 9.386 and, respectively, 34 GHz. The temperature was varied between 3 and 300 K. For the photo-EPR studies, CW semiconductor lasers were used with the excitation energies of 1.94 and 3.06 eV. Rabi oscillations were measured by the Fourier-transform (FT) EPR technique at the X-band frequency of about 9.78 GHz. The electron-spin-echo detected EPR spectra were obtained by monitoring the intensity of the Hahn echo as a function of the external magnetic field.

The PL of the iron centers was excited by the semiconductor laser with 3.06-eV photon energy. The PL spectra were measured by a triple-spectrometer equipped with a liquid nitrogen-cooled charge-coupled device camera. In the additive mode, the spectrometer had a total focal length of 1.5 m and a spectral resolution of approximately 30 μeV (0.25 cm^{-1}) for a slit width of 10 μm [28]. The Zeeman splitting was measured in external magnetic fields B up to 10 T generated by a superconducting split-coil solenoid. The propagation directions of the incident and emitted light were parallel (Faraday geometry) or perpendicular (Voigt geometry) to **B**. The angular dependencies of the Zeeman splittings were measured by rotating the sample in the crystal planes $(1\bar{2}10)$ and (0001) with respect to **B**.

III. CW-EPR SPECTRA

The EPR technique provides information on the ground state of the iron centers in ZnO. An EPR spectrum of the ZnO sample with low iron concentration is shown in Fig. 1(a) measured in dark, a magnetic field applied along the crystal c axis. For the X-band microwave frequency of 9.386 GHz, three sets of strong Fe^{3+}-related EPR signals can be identified. They belong to three types of charge-compensated Fe^{3+} centers whose compensation is provided by neighboring Li$^+$ ions [10]: (i) Fe^{3+}-Li(I) with the iron ion at an axial Zn site and a lithium ion at one of the nearest six cationic sites lying in the basal (0001) plane; (ii) Fe^{3+}-Li(II) with a Li$^+$ ion at one of the cationic positions that form a trigonal prism; and (iii) Fe^{3+}-Li(III) with Fe^{3+} substituted for one of the six cationic sites and Li$^+$ at an axial Zn site.

Recent electron-nuclear double-resonance (ENDOR) measurements by Kutin *et al.* [29] reveal nuclear magnetic resonance transitions that correspond to Li nuclei acting as charge compensators.

ZnO has a wurtzite crystal lattice with C_{6v}^4 symmetry. An iron ion in ZnO acts as a deep neutral donor and is
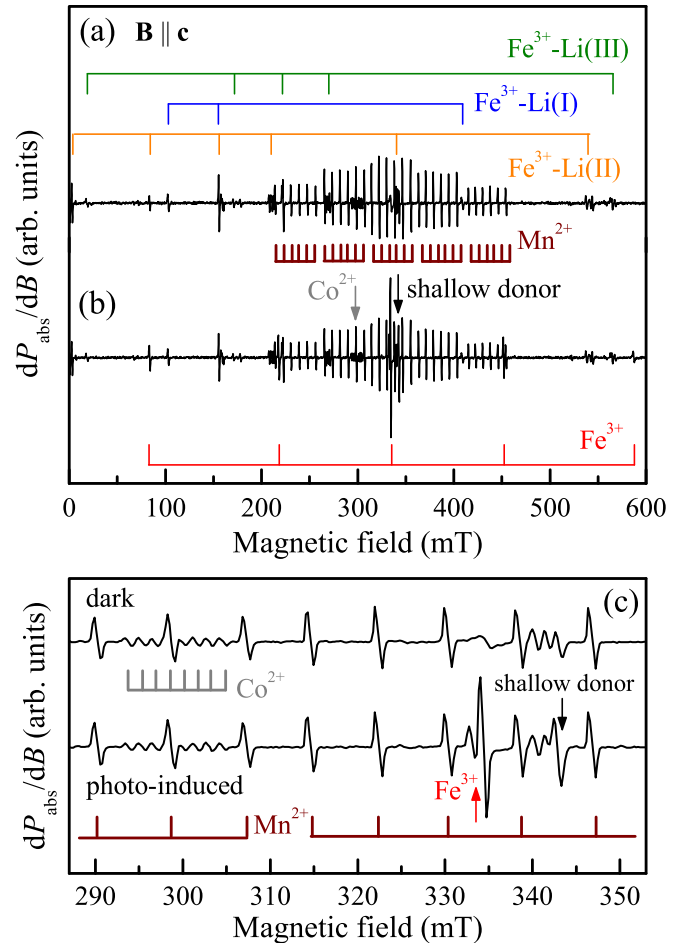

FIG. 1. (Color online) (a) Dark EPR spectrum measured at $T = 9.5$ K and a microwave frequency of 9.386 GHz. The applied magnetic field is parallel to the c axis of the crystal. Three types of charge-compensated Fe^{3+} centers are identified, beside the EPR signals of Mn^{2+} and Co^{2+}. (b) Photo-EPR spectrum containing the signals of trigonal Fe^{3+} centers and shallow donors (under illumination with 1.94 eV laser light). (c) Detailed view of dark and photo-EPR spectra in a narrow applied magnetic field range. The shallow donor with $g = 1.956$ is indicated by the arrow.

typically present in the divalent state Fe^{2+}. Due to the large zero-field splitting one cannot expect to observe an EPR signal of the Fe^{2+} ion in ZnO [30]. The Fe^{3+} ions can substitute for Zn^{2+} in two cationic positions that are tetrahedrally coordinated by four oxygen ions. The second ligand shell of the crystal contains twelve zinc ions, six of them form a trigonal prism. The local crystal field of the iron impurity is described by two contributions: the axial crystal-field distortion because of the polar structure of ZnO, and the distortion caused by the presence of an additional point charge in the vicinity of the Fe^{3+} ion. The latter case can be realized by a charge compensator, such as Li$^+$ incorporated at a crystallographically different sites. The presence of a Li$^+$ ion in the second- or third-cationic shell of Fe^{3+} leads to its local charge compensation thus forming a neutral associated defect [10].

The EPR spectum in the dark condition contains only very weak signals of the Fe^{3+} center in a regular lattice environment

(with trigonal symmetry). Its EPR signal can be photoinduced at $T = 9.5$ K by optical excitation with 1.94-eV photon energy. In Figs. 1(b) and 1(c), the five allowed fine-structure transitions due to the electron spin $S = 5/2$ are demonstrated. The appearance of these lines can be attributed to the charge conversion of Fe^{2+} to Fe^{3+} due to the electron ionization of isolated Fe^{2+} ions. After photoexcitation, the trigonal Fe^{3+} centers remain stable at low temperature. The photoinduced changes can be reversed by heating the sample above 90 K, so that the Fe^{3+} centers are converted back to the divalent charge state.

The EPR spectra for the different types of Fe^{3+} centers can be described by the following spin Hamiltonian with inversion symmetry C_i only:

$$H = g \, \mu_B \, \mathbf{B} \cdot \mathbf{S} + \sum_{m=-l}^{l} B_{lm} \overline{O}_m^l,$$ (1)

where

$$\overline{O}_0^l = T_0^l, \quad \overline{O}_m^l = \left[T_{-m}^l + (-1)^m T_m^l \right],$$

$$\overline{O}_{-m}^l = i \left[T_{-m}^l - (-1)^m T_m^l \right],$$

where μ_B is the Bohr magneton, the vector $\mathbf{B}(B_x, B_y, B_z)$ of the external magnetic field is defined in orthohexagonal crystallographic axes, the electron Zeeman g factor is given by g, and T_m^l are spherical tensor operators [31–34]. The scalar fine-structure parameters B_{lm} are given by $B_{20} = (2/\sqrt{6})b_2^0$, $B_{2\pm1} = (1/6)b_2^{\pm1}$, $B_{2\pm2} = (1/3)b_2^{\pm2}$, $B_{40} = (\sqrt{70}/30)b_4^0$, and $B_{43} = (\sqrt{2}/120)b_4^3$. Here, b_l^m are Stevens coefficients.

The angular dependent positions of the EPR fine-structure lines for the charge-compensated Fe^{3+} centers are shown in Fig. 2. The magnetic field direction was varied in the (0001) plane of the ZnO crystal. Circles are experimental values measured at microwave frequency of 34 GHz. The lines show fitting results using the spin Hamiltonian of Eq. (1). The magnetic multiplicity of the corresponding EPR spectra is designated by K_M [35]. This is the minimal number of physically equivalent, but magnetically nonequivalent coordinate systems, in which the spin Hamiltonian tensors of second and fourth ranks are defined. The alignment of the crystal with respect to the magnetic field direction is critical because of the presence of low-symmetry effects, such as the noncoinciding extrema of different fine-structure transitions and the angular dependence asymmetry for the large number of magnetically nonequivalent centers. The spin Hamiltonian parameters evaluated from the fit of the experimental data are listed in Table I together with those of the trigonal Fe^{3+} center [9,11,12]. The parameters of the Fe^{3+}-Li(I) and Fe^{3+}-Li(II) centers are defined in a coordinate systems that makes b_2^0 negative, while b_2^0 for Fe^{3+}-Li(III) is positive. In the case of trigonal Fe^{3+} centers, the sign of b_2^0 is negative [9]. The coordinate systems for all magnetically nonequivalent Fe^{3+} centers are related by the twelve symmetry elements of the rotation group D_6.

IV. ELECTRON-SPIN ECHO STUDIES

The trigonal Fe^{3+} center ($S = 5/2$) is one of the simplest magnetic systems, with a well-defined crystalline anisotropy
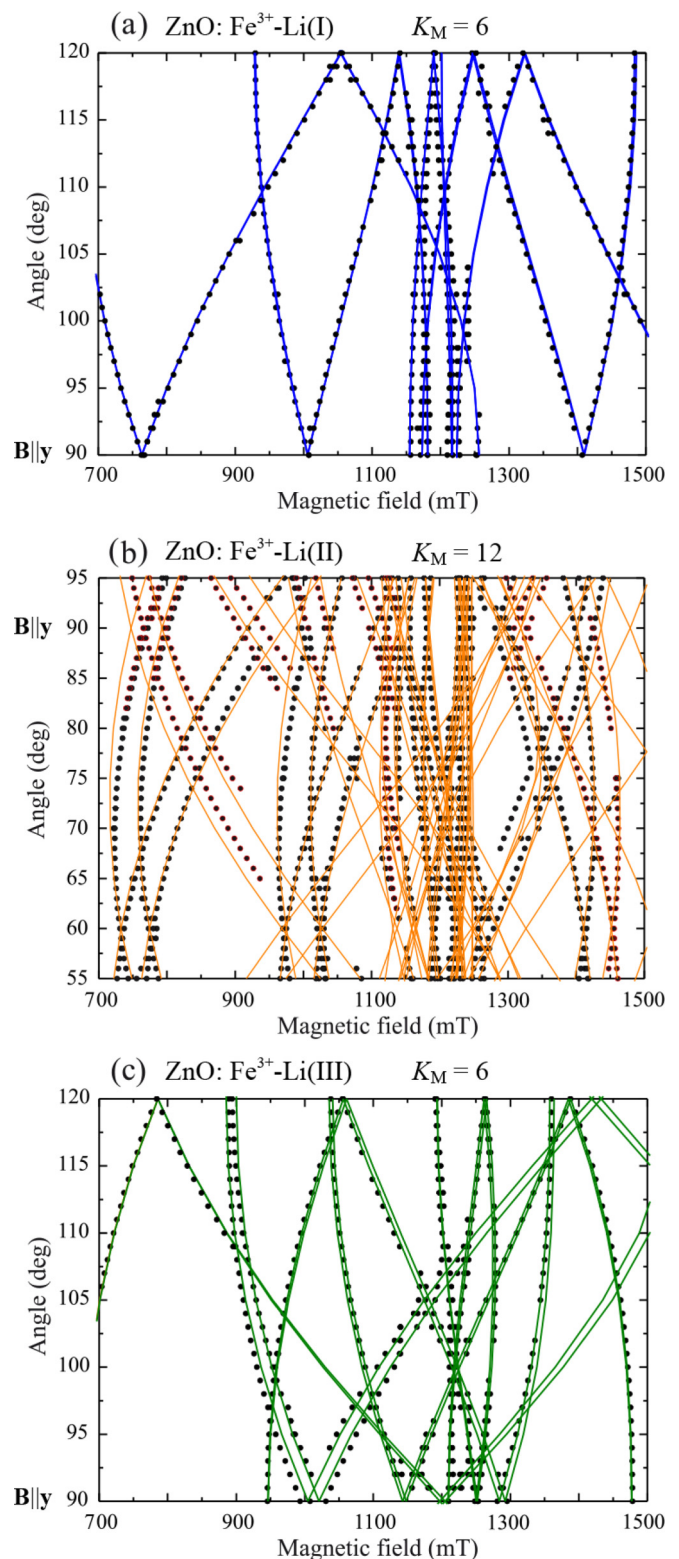

FIG. 2. (Color online) Angular dependence of resonance fields for (a) Fe^{3+}-Li(I), (b) Fe^{3+}-Li(II), and (c) Fe^{3+}-Li (III) centers in ZnO when the applied magnetic field sweeps in (0001) plane. The magnetic multiplicity of the EPR spectra in the ZnO structure is designated by K_M.

[9,11] in a ZnO matrix containing a limited number of nuclear spins. A corresponding EPR spectrum is shown in Fig. 3(a).

TABLE I. Spin Hamiltonian parameters of the trigonal and charge-compensated Fe^{3+} centers in ZnO single crystals (in 10^{-4} cm^{-1}, $T = 300$ K).

m	b_2^m	b_4^m	g	Ref.
	Fe^{3+}			
0	−595.0	−12.3	2.006	[9,11]
3		−390.0		
	Fe^{3+}-Li(I)			
0	−1282.0	−14.0	2.006	[12]
2	1347.0			
3		390.0		
	Fe^{3+}-Li(II)			
0	−796.0	−11.0	2.006	[12]
1	−621.0			
2	−1085.0			
−1	−2006.0			
−2	771.0			
3		−390.0		
	Fe^{3+}-Li(III)			
0	490.0	−14.0	2.006	[12]
1	−980			
2	2035			
3		−390.0		

The observed EPR resonance linewidth of trigonal Fe^{3+} for an applied magnetic field **B**∥**c** is varying from 0.085 to 0.095 mT at a temperature of $T = 30$ K. The pronounced anisotropy of the EPR spectra of trigonal Fe^{3+} is due to the
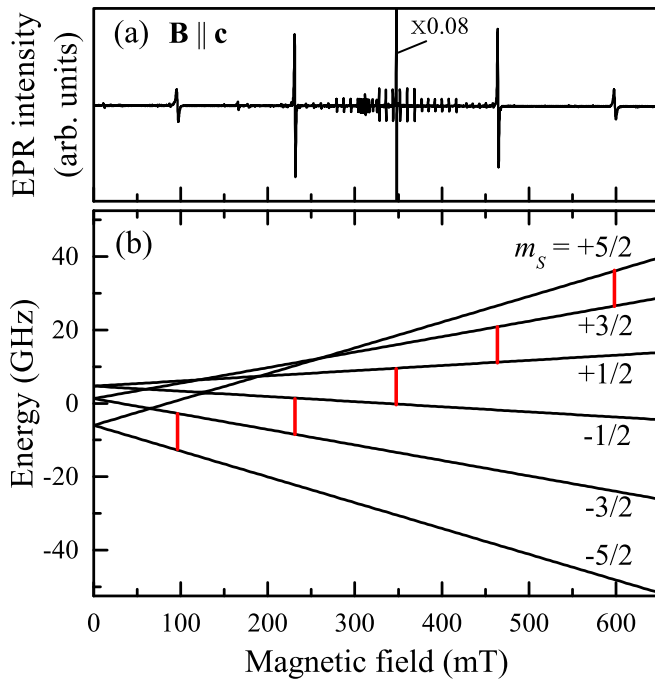

FIG. 3. (Color online) (a) EPR spectrum of trigonal Fe^{3+} center for **B** ∥ **c**, $T = 30$ K, and microwave frequency of 9.75 GHz. The EPR signal of the transition $|-1/2\rangle \leftrightarrow |1/2\rangle$ is scaled by the factor of 0.08. (b) Corresponding ground-state energy-level scheme. Allowed transitions with $\Delta m_s = \pm 1$ are shown by vertical lines.

second and fourth rank fine structure tensors describing the ground-state energy level splitting:

$$H = g\mu_B \mathbf{B} \cdot \mathbf{S} + B_{20}\overline{O}_0^2 + B_{40}\overline{O}_0^4 + B_{43}\overline{O}_3^4. \quad (2)$$

The spin Hamiltonian (2) includes the Zeeman term and the crystal-field potential of C_{3v} symmetry. The five allowed fine-structure transitions ($\Delta M = \pm 1$) are shown in Fig. 3(b) for **B**∥**c** at an operating microwave frequency of 9.75 GHz. The cubic anisotropy arising from the $\overline{O}_3^4$ tesseral tensor operator can be compensated by the alignment of the applied magnetic field parallel to the c-axis direction. In this case, the corresponding spin states are well defined. Therefore the ground-state spin dynamics of longitudinal magnetization $\langle S_z \rangle$ can be easily tuned for **B**∥**c**.

Rabi oscillations were measured using the electron spin echo (ESE) technique in hydrothermal grown ZnO sample doped with Fe^{3+} ions at a concentration of approximately 10^{20} cm^{-3}. In our experiments, Rabi oscillations in the trigonal Fe^{3+} system were observed by application of a nutation (pump) pulse followed by a $\pi/2 - \pi$ sequence after a delay time $\tau_0 \gg T_2$.

The one-photon Rabi oscillation frequency between the M and $M+1$ states involved in the transition is the following [24,36]:

$$\Omega_R = \tfrac{1}{2}g\mu_B B_1 \sqrt{S(S+1) - M(M+1)}/h. \quad (3)$$

One-photon transitions dominate [23] when the applied magnetic field is along the primary crystal direction (**B**∥**c**, in our case). Rabi oscillation measurements are performed by application of a static magnetic field at the $-1/2 \leftrightarrow 1/2$ resonance. The coherent spin nutation is shown in Fig. 4(a). The oscillation frequencies are obtained by a fast Fourier Transform (FFT) of the detected Rabi oscillations [36]. Figure 4(b) shows a precise agreement between the experiment and the calculated curve expected for a one-photon process [see Eq. (3)].

By use of two-pulse electron spin echo decay measurements, we found the value of phase memory time of $T_2^a \approx 6.055$ μs at the temperature of 60 K and of $T_2^b \approx 19.115$ μs at the temperature of $T = 30$ K. Fitting is to $A(t) = A_o\,e^{-(t/T_2)}$.

The time dependence of the Rabi oscillations can be represented by use of a damping time τ_R smaller than T_2 by the equation [36,37]:

$$\langle S_z\rangle(t) = S_z\,|_{t=0}\,e^{-t/\tau_R}\cos(\Omega_R t), \quad (4)$$

where Ω_R is the Rabi frequency obtained from FFT of the experimental data. The Rabi frequency dependence of the decoherence rate $1/\tau_R$ exhibits an approximately linear decrease and can be represented as follows [38,39]:

$$\frac{1}{\tau_R} = \beta\frac{\Omega_R}{2\pi} + \frac{1}{2T_2}, \quad (5)$$

where β is the proportionality constant and $1/T_2$ is the coherence time. The dependence of the damping rate $1/\tau_R$ presented in Fig. 5(b) exhibits an approximate fit to Eq. (5) characterizing the influence of spin-bath decoherence mechanism.
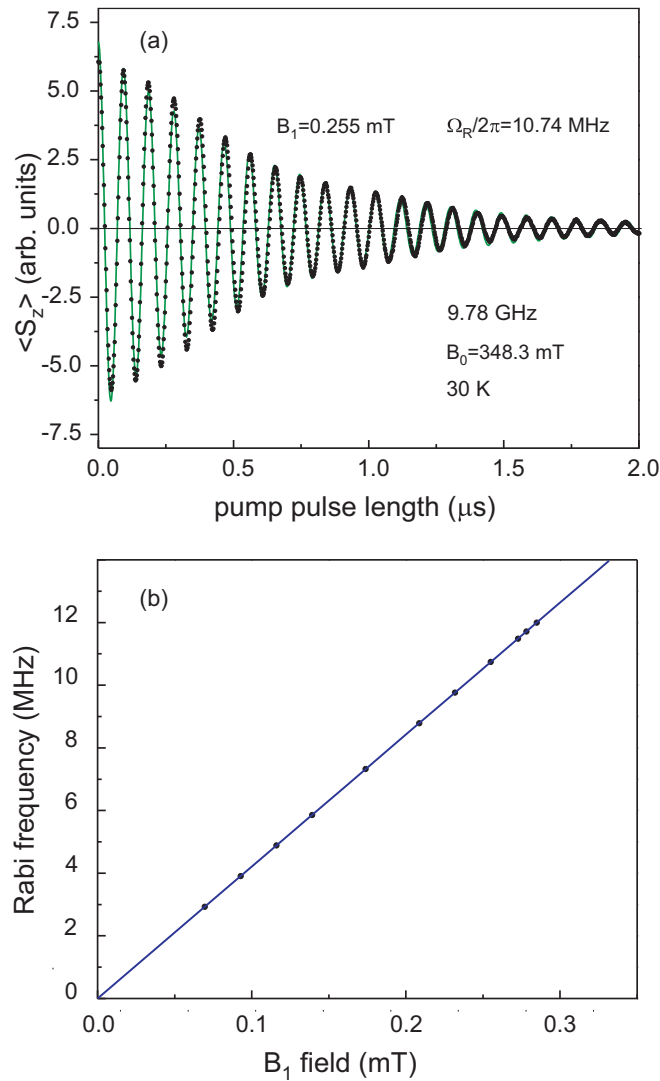
FIG. 4. (Color online) (a) Time dependence of $\langle S_z \rangle$ fitted by Eq. (4), $T = 30$ K. (b) Rabi frequencies plotted as function of the amplitude of the microwave field. The dependence expected for the one-photon oscillation frequency is indicated by the line.
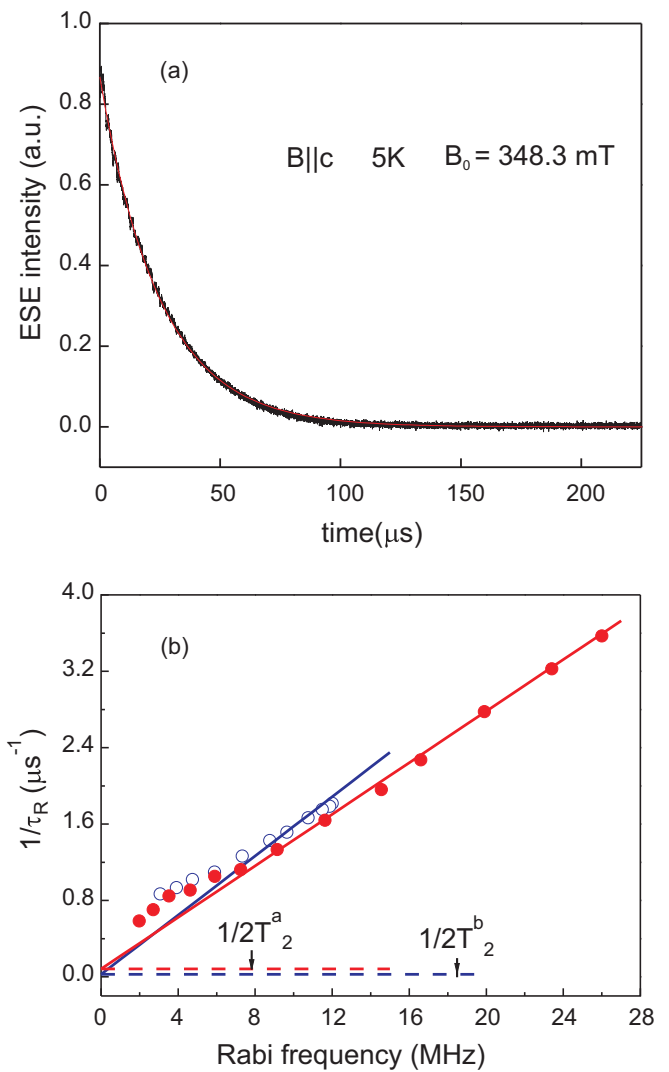

FIG. 5. (Color online) (a) Electron spin echo decay for the $|-1/2\rangle \leftrightarrow |+1/2\rangle$ transition at the temperature of 5 K. Phase memory time fitted is $T_M = 24.77$ μs. (b) Dependence of the damping rate $1/\tau_R$ of Rabi oscillations vs Rabi frequency at the temperatures of 30 and 60 K. The solid lines are the approximate fit to spin-bath decoherence mechanism described by Eq. (5).

It appears that Fig. 5(b) provides peculiar region at low Rabi frequencies, primarily in the vicinity of ^{6}Li (natural abundance of 7.59%, nuclear spin of $I = 1$), ^{7}Li (natural abundance of 92.41%, nuclear spin of $I = 3/2$). We attribute observed decoherence mechanism to the electron-nuclear spin cross-relaxation in the rotating frame.

V. MAGNETOPHOTOLUMINESCENCE

A photoluminescence spectrum of trigonal Fe^{3+} centers in ZnO at zero magnetic field is shown in Fig. 6. The linearly polarized photoluminescence was measured with **E** parallel or perpendicular to the crystal c-axis. Sharp zero-phonon lines (ZPLs) are detected at about 1.788 eV and a strong phonon sideband at lower energy. The energy differences ΔE of the phonon replicas from the ZPL A at 1.78801 eV are

indicated. The vibronic sideband of the sharp zero-phonon lines illustrates the dominant coupling to acoustic phonons with a phonon energy of 12.8 meV. The strongest replica is at 1.72441 eV. Due to its narrow linewidth it can be assigned to the local phonon mode which is localized in the vicinity of the Fe^{3+} ion.

The ZPLs denoted by A, B, C, and D are depicted in detail in Fig. 7(a). The observed emission band is attributed to the spin-forbidden electric-dipole transition from the excited state $^4T_1(G)$ to the ground state $^6A_1(^6S)$ of the Fe^{3+} center [16,40,41]. The Fe^{3+} ion site is not at the center of inversion; hence, the electric-dipole transitions within the $3d$ shell are partially allowed by the mixing of states with different parity through the odd crystal-field components.

Due to the strong thermalization of the different ZPLs, as shown in Fig. 7(a), the most PL studies were performed at an
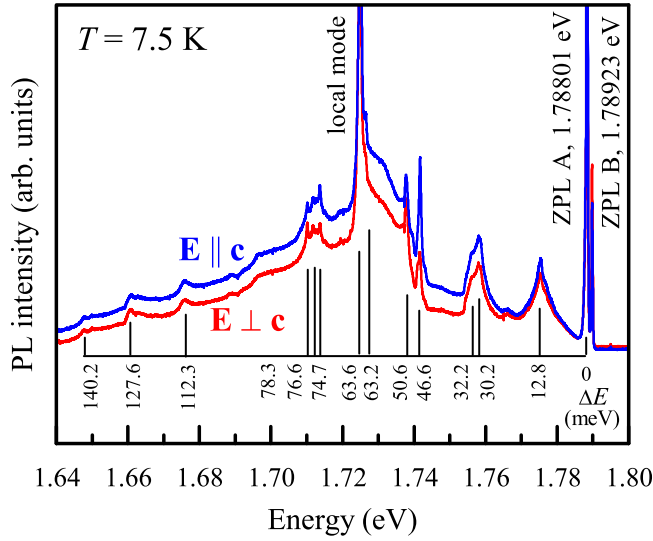
FIG. 6. (Color online) Polarized PL band assigned to Fe^{3+} intracenter transitions, $B = 0$ T. The energy differences for phonon sideband replicas are noted.

FIG. 8. (Color online) Zeeman structure of the zero-phonon PL lines when the applied magnetic field is orthogonal to c axis of the ZnO crystal (Voigt geometry).

elevated temperature of 7.5 K. The PL intensities of the ZPLs A, B, and D as well as the full width at half maximum (FWHM) of the ZPL A are depicted as a function of the temperature in
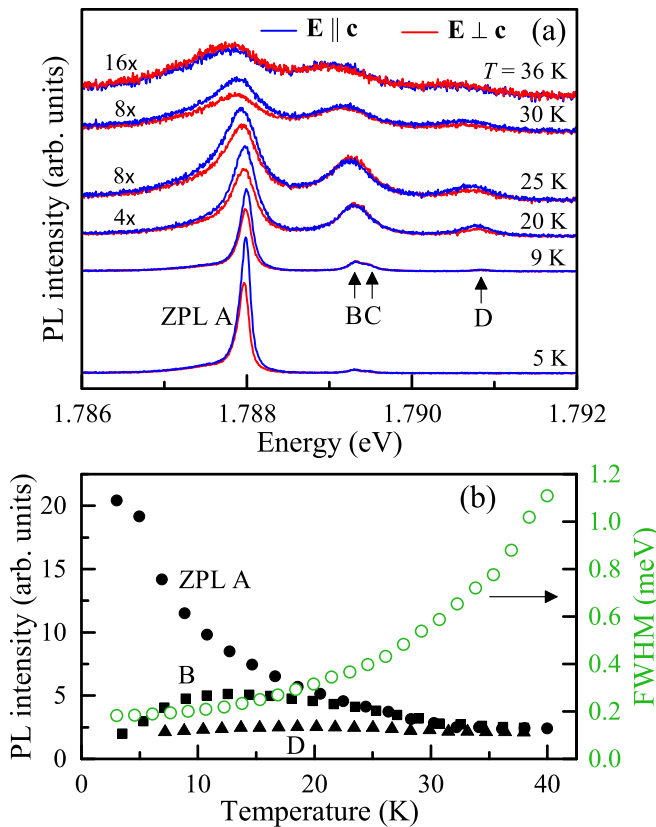

FIG. 7. (Color online) (a) Polarized PL spectra of the ZPLs for $B = 0$ T measured at different temperatures. The corresponding temperature dependencies of the integral PL intensities (solid symbols) and of the FWHM of the ZPL A (open circles) are depicted in (b).
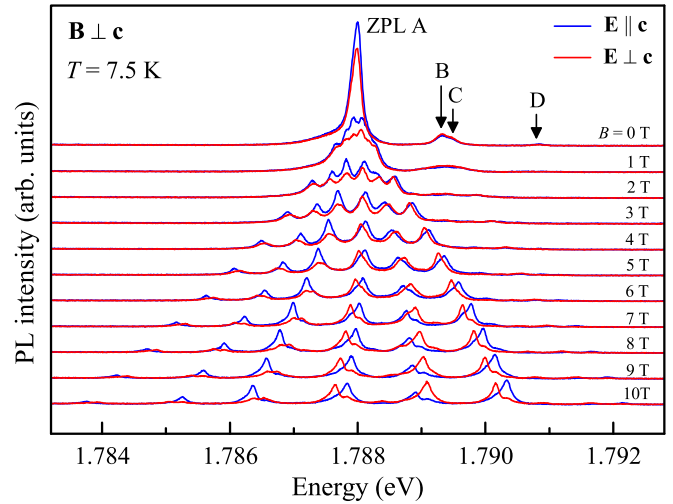
Fig. 7(b). Note that the direct phonon processes have been determined to be more important for the low lying levels of $^4T_1(G)$ term at low temperatures [16].

Figure 8 shows the experimental magnetic field dependence of the polarized ZPLs. The applied magnetic field is orthogonal to the trigonal c axis. The spectra demonstrate a sixfold splitting of the ZPL A and its strong nonlinearity with increasing magnetic field. The splitting corresponds to transitions from the $\Gamma_{5/6}$ level to the $2S + 1$ ground-state energy levels with electron spin $S = 5/2$. As it can be seen in high magnetic fields, each line is further split into a doublet with different linear polarization. This is due to the splitting of the $\Gamma_{5/6}$ excited state. The Zeeman pattern of the ZPLs exhibits the characteristic removal of the Kramers' doublet degeneracy of the $^6A_1$ ground state. Therefore we use the spin Hamiltonian (2) with C_{3v} symmetry to describe the ground-state energy splitting of the trigonal Fe^{3+} centers. The g factor of 2 and the trigonal field parameter $b_2^0 = 0.06$ cm^{-1} (≈ 7.44 μeV) are taken into account to evaluate the $^6A_1$ ground-state zero-field splitting. These parameters are in reasonable agreement with the EPR data related to the photogenerated trigonal Fe^{3+} centers in the ZnO crystals.

In the following, we consider the excited states related to $^4T_1$ under action of the crystal field and the Zeeman effect. The cubic crystal field splits the free ion ^4G state into two excited orbital triplet states $^4T_2$ and $^4T_1$. They further split into states with the total angular momentum $\mathbf{J} = \mathbf{S} + \mathbf{L}$ due to the first-order spin-orbit interaction. The irreducible representations of the excited states are given by Γ_7 with $J = 1/2$, Γ_8 with $J = 3/2$, and $\Gamma_6 + \Gamma_8$ with $J = 5/2$. We use the effective orbital momentum $L = 1$ to describe T_1 state [42]. In presence of an external magnetic field the states with different total angular momenta can be characterized by the effective Landé factor

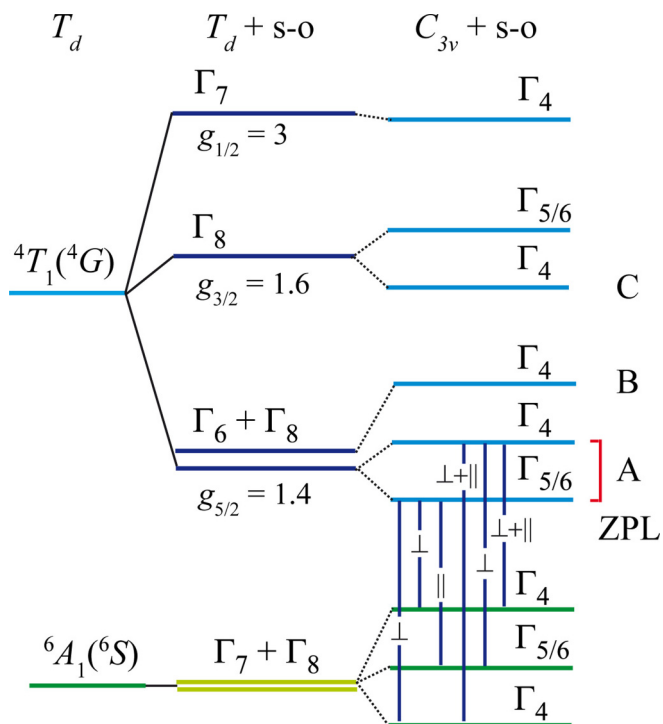$$g_J = \frac{1}{2}(g_S + g_L) + \frac{1}{2}(g_S - g_L)\frac{S(S+1) - L(L+1)}{J(J+1)}, \quad (6)$$

FIG. 9. (Color online) Diagram of the ground- and excited-state energy levels of Fe^{3+} in T_d and C_{3v} fields, accounting for the spin-orbit (s-o) coupling. The transitions from the exited states giving rise to the ZPLs are designated by A, B, and C. The selection rules are indicated for some of the transitions to the ground-state $^6A_1$ term.

FIG. 10. (Color online) Zeeman splitting of the ZPLs A, B, and C assigned to the $^4T_1 \rightarrow {}^6A_1$ transition of the Fe^{3+} center, $T = 7.5$ K. The applied magnetic field is orthogonal (a) or parallel (b) to **c**. Experimental data are indicated by circles. The simulated curves represent calculations with Eqs. (2) and (7).

where g_L and g_s are the gyromagnetic ratios for the orbital and spin angular momentum [43]. For the $^4T_1$ state originating from ^4G it can be shown that $g_L = 1/2$. The corresponding effective g_J values are designated in Fig. 9, where the ground- and excited-state energy levels of Fe^{3+} are schematically depicted. The symmetry assignments of the levels and their ordering correspond to the simulated Zeeman fine structure, which are shown in Fig. 10. The sixfold $J = 5/2$ level, the lowest one in energy, is split by second-order spin-orbit coupling into a Γ_6 doublet and a Γ_8 quartet in T_d. The zero-phonon emission line A observed at low temperatures stems from the $\Gamma_8(^4T_1)$ excited state. The low lying Γ_8 quartet with an effective angular momentum of $J = 3/2$ split into two doublet states with a doublet Γ_4 lying above the $\Gamma_{5/6}$ states.

Figure 9 also demonstrates the allowed E1 (electric-dipole) transitions and their characteristic polarizations with $\mathbf{E} \parallel \mathbf{c}$ or $\mathbf{E} \perp \mathbf{c}$ for the ZPL A. The selection rules for the polar vectors in C_{3v} symmetry of the Zn sites are presented in the following: the E1 transitions between Γ_4 and Γ_4 are allowed with $\mathbf{E} \parallel \mathbf{c}$ as well as $\mathbf{E} \perp \mathbf{c}$. The transitions from Γ_4 to $\Gamma_{5/6}$ are characterized by $\mathbf{E} \perp \mathbf{c}$, and those from $\Gamma_{5/6}$ to $\Gamma_{5/6}$ by $\mathbf{E} \parallel \mathbf{c}$.

The zero-phonon lines B and C are observed at 1.78923 and 1.78940 eV, respectively. They are attributed to transitions from the Γ_4 doublets originating from states with either $J = 5/2$ or $J = 3/2$. The most general Hamiltonian for impurity centers with local symmetry of C_{3v} and a total angular momentum of $J = 3/2$ is given by
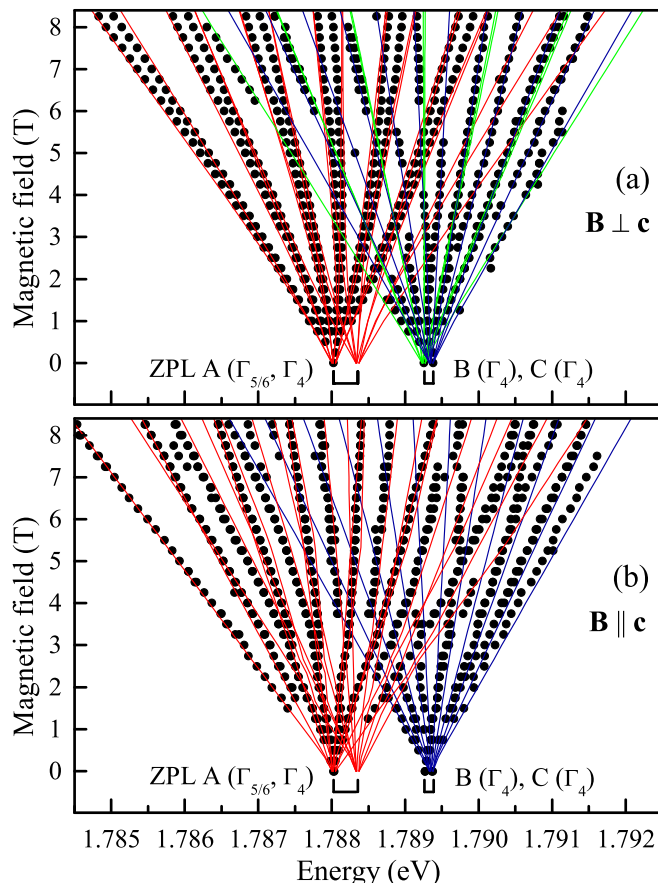
$$H = g\,\mu_B\,\mathbf{B} \cdot \mathbf{J} + v_0^{312}\,V_0^{312} + B_{20}\,\overline{O}_0^2 \qquad (7)$$

with the scalar coefficient v_0^{312}. The high-rank Zeeman term

$$V_0^{312} = \mu_B\big[\sqrt{3}B_z\,\overline{O}_0^3 + \big(B_x\,\overline{O}_1^3 + B_y\,\overline{O}_{-1}^3\big)\big]/\sqrt{7}$$

has the dimension of $\mathbf{B}\mathbf{J}^3$ as defined in Ref. [32]. We suggest that the effective Hamiltonian, Eq. (7), is acting within Γ_4 and $\Gamma_{5/6}$ states in C_{3v}. The importance of the Zeeman term containing the third-rank tensor spin-operators to describe the Zeeman effect of a Γ_8 quartet state was shown by Bleaney [44] as well as Koster and Statz [45]. The Zeeman splitting of the ZPLs A, B, and C are shown in Fig. 10 for the Voigt (a) and Faraday (b) configuration. The narrow linewidths of the ZPLs of approximately 150 μeV allow us to estimate the fine structure of the ground and excited states involved in the electric-dipole transitions. The experimental peak positions of

TABLE II. Calculated effective Hamiltonian parameters for the excited states of the trigonal Fe^{3+} center in ZnO.

ZPL	J	g	b_2^0 (cm^{-1})	v_0^{312}
A ($\Gamma_{5/6}$, Γ_4)	3/2	1.4	−1.3	0.6
B (Γ_4)	1/2	2.0	–	–
C (Γ_4)	1/2	1.0	–	–

the observed Zeeman lines are indicated by circles and the simulated curves [the modeling based on the Eqs. (2) and (7)] by solid lines. The parameters for the calculations are presented in Table II. The reduction in symmetry to the C_s and to the C_3 point groups occurs when the applied magnetic field is orthogonal to the optical c-axis and for **B**∥**c**, respectively [46]. The theoretical polarization selection rules are in agreement with the observed polarizations of the ZPL A.

Our magneto-optical measurements at $B = 8$ T do not exhibit any angular dependence of the Fe^{3+} ZPLs when the magnetic field is applied in the (0001) plane of the ZnO crystal. This lack of angular dependence is expectable for the C_{3v} symmetry. In the case of magnetic field rotation within the $(1\bar{2}10)$ plane the Zeeman components change their energy positions, as it is shown in Fig. 11. The Zeeman components of the ZPL A are associated with transitions from the Γ_4 and $\Gamma_{5/6}$ levels to the six ground-state levels with $S = 5/2$. This is evidenced in the angular variation of the Zeeman spectra. Two sets of solid lines represent the calculated angular dependence of magnetically nonequivalent Fe^{3+} centers with magnetic multiplicity $K_M = 2$. The coordinate systems for the two magnetically nonequivalent Fe^{3+} centers, located at the cationic site-symmetry positions A and B, are related by a 60° rotation (C_3 symmetry operation) about the c axis. The
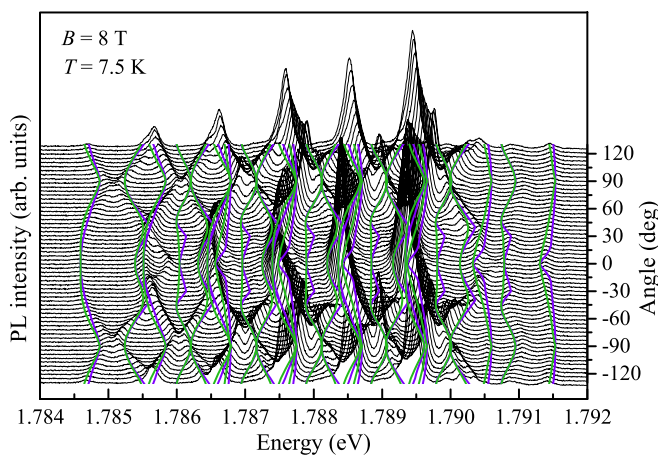

FIG. 11. (Color online) Angular variation of the Zeeman sublevels related to the ZPLs A, B, and C. The applied magnetic field $B = 8$ T was rotated within the $(1\bar{2}10)$ plane. The angle of 0° corresponds to **B** ∥ **c**. The simulated curves, shown above the experimental spectra, correspond to the ZPL A. The magnetic multiplicity of the Zeeman spectra is $K_M = 2$. Two magnetically nonequivalent centers are designated by the simulated curves of different color.

behavior of the low-lying $\Gamma_8(^4T_1)$ excited state is described by the Hamiltonian, Eq. (7), with an effective angular momentum of $J = 3/2$. The pronounced cubic anisotropy is due to the anisotropy of the excited Γ_8 state, whereas the anisotropy of the ground state is too small to be optically detectable. The Γ_4 excited-state doublets related to the ZPLs B and C are determined by considering the linear Zeeman term only and an effective angular momentum $J = 1/2$. The calculated curves in the angular dependent Zeeman pattern are obtained by taking the eigenvalue differences of the Hamiltonians [Eqs. (2) and (7)] acting in the space of states of the ground and excited multiplets of the Fe^{3+} center with C_{3v} point symmetry. No significant distortion of the C_{3v} symmetry was detected, as may be expected from the Jahn-Teller effect, namely, from the electron-vibrational coupling of an orbitally degenerate state [47,48].

VI. CONCLUSIONS

The analysis of the magnetic field effect on the $^4T_1(G)$ state of Fe^{3+} in ZnO allows us to reconsider the scheme of the lowest lying fine-structure lines. For that purpose, well-resolved polarized PL spectra (**E** ∥ **c** and **E** ⊥ **c**) are analyzed. The Zeeman components of the most intense zero-phonon line A in the PL spectra are associated with transitions from the lowest excited $\Gamma_8(^4T_1)$ state to the ground state with $S = 5/2$. We demonstrate that the observed fine structure of the $\Gamma_8(^4T_1) \rightarrow {}^6A_1(^6S)$ transition of Fe^{3+} is primarily affected by second-order spin-orbit interaction and spin-spin interaction. The detailed measurement of the angular variation of the Zeeman PL lines indicates two magnetically nonequivalent centers that are related to two cationic site symmetry positions A and B in the wurtzite lattice. The latter is taken into account by the high-rank Zeeman term V_0^{312}, which leads to a cubiclike angular dependence. The studies of the optical spectra provide information on the electronic transitions of Fe^{3+} centers in ZnO, which complements the results obtained from EPR and photo-EPR experiments. We use EPR to monitor photoinduced changes in the charge states of donors in hydrothermally grown single ZnO crystals. We demonstrate that the EPR spectra of trigonal Fe^{3+} ions and shallow donors can be photogenerated with below band-gap laser excitation. We further investigate the decoherence of the Rabi oscillations in the trigonal Fe^{3+} system via different amplitudes of the applied microwave field. The spin dynamics of the Fe^{3+} ions are controlled by recording the one-photon Rabi oscillations for a magnetic field applied along the c axis. The observed decoherence mechanism is related to the electron-nuclear spin cross-relaxation in the rotating frame.

[1] C. Klingshirn, Phys. Stat. Sol. (b) **244**, 3027 (2007).

[2] H. Sezen, H. Shang, F. Bebensee, C. Yang, M. Buchholz, A. Nefedov, S. Heissler, C. Carbogno, M. Scheffler, P. Rinke, and C. Wöll, Nat. Commun. **6**, 6901 (2015).

[3] K. Nomura, H. Ohta, K. Ueda, T. Kamiya, M. Hirano, and H. Hosono, Science **300**, 1269 (2003).

[4] Ü. Özgür, Y. I. Alivov, C. Liu, A. Teke, M. A. Reshchikov, S. Doğan, V. Avrutin, S. J. Cho, and H. Morkoc, J. Appl. Phys. **98**, 041301 (2005).

[5] D. M. Hofmann, A. Hofstaetter, F. Leiter, H. Zhou, F. Henecker, B. K. Meyer, S. B. Orlinskii, J. Schmidt, and P. G. Baranov, Phys. Rev. Lett. **88**, 045504 (2002).

[6] S. B. Orlinskii, J. Schmidt, P. G. Baranov, D. M. Hofmann, C. de Mello Donega, and A. Meijerink, Phys. Rev. Lett. **92**, 047603 (2004).

[7] B. K. Meyer, H. Alves, D. M. Hofmann, W. Kriegseis, D. Forster, F. Bertram, J. Christen, A. Hoffmann, M. Straßburg, M. Dworzak, U. Haboeck, and A. V. Rodina, Phys. Stat. Sol. (b) **241**, 231 (2004).

[8] F. A. Selim, M. H. Weber, D. Solodovnikov, and K. G. Lynn, Phys. Rev. Lett. **99**, 085502 (2007).

[9] J. Schneider, Z. Naturforschg. **17a**, 189 (1962).

[10] W. C. Holton, M. de Wit, T. L. Estle, B. Dischler, and J. Schneider, Phys. Rev. **169**, 359 (1968).

[11] W. M. Walsh and L. W. Rupp, Phys. Rev. **126**, 952 (1962).

[12] D. V. Azamat and M. Fanciulli, Physica B **401–402**, 382 (2007).

[13] T. E. Mølholt, H. P. Gunnlaugsson, K. Johnston, R. Mantovan, H. Masenda, D. Naidoo, S. Olafsson, K. Bharuth-Ram, H. P. Gislason, G. Langouche, R. Sielemann, and G. Weyer, Phys. Scr. **T148**, 014006 (2012).

[14] V. A. Nikitenko, J. Appl. Spectrosc. **56**, 783 (1994).

[15] Yongquan Jiang, N. C. Giles, and L. E. Halliburton, J. Appl. Phys. **101**, 093706 (2007).

[16] R. Heitz, A. Hoffmann, and I. Broser, Phys. Rev. B **45**, 8977 (1992).

[17] M. N. Leuenberger and D. Loss, Nature (London) **410**, 789 (2001).

[18] M. N. Leuenberger, D. Loss, M. Poggio, and D. D. Awschalom, Phys. Rev. Lett. **89**, 207601 (2002).

[19] S. Bertaina, S. Gambarelli, T. Mitra, B. Tsukerblat, A. Müller, and B. Barbara, Nature **453**, 203 (2008).

[20] M. V. G. Dutt, L. Childress, L. Jiang, E. Togan, J. Maze, F. Jelezko, A. S. Zibrov, P. R. Hemmer, and M. D. Lukin, Science **316**, 1312 (2007).

[21] E. Baibekov, I. Kurkin, M. Gafurov, B. Endeward, R. Rakhmatullin, and G. Mamin, J. Magn. Reson. **209**, 61 (2011).

[22] A. Morello, P. C. E. Stamp, and I. S. Tupitsyn, Phys. Rev. Lett. **97**, 207206 (2006).

[23] S. Bertaina, L. Chen, N. Groll, J. Van Tol, N. S. Dalal, and I. Chiorescu, Phys. Rev. Lett. **102**, 050501 (2009).

[24] S. Bertaina, N. Groll, L. Chen, and I. Chiorescu, Phys. Rev. B **84**, 134433 (2011).

[25] H. De Raedt, B. Barbara, S. Miyashita, K. Michielsen, S. Bertaina, and S. Gambarelli, Phys. Rev. B **85**, 014408 (2012).

[26] S. T. Ochsenbein and D. R. Gamelin, Nat. Nanotechnol. **6**, 112 (2011).

[27] J. Tribollet, J. Behrends, and K. Lips, Europhys. Lett. **84**, 20009 (2008).

[28] J. Debus, D. Dunker, V. F. Sapega, D. R. Yakovlev, G. Karczewski, T. Wojtowicz, J. Kossut, and M. Bayer, Phys. Rev. B **87**, 205316 (2013).

[29] Yu. S. Kutin, G. V. Mamin, and S. B. Orlinskii, J. Magn. Reson. **237**, 110 (2013).

[30] W. Gehlhoff, D. Azamat, A. Hoffmann, N. Dietz, and O. V. Voevodina, Physica B **376–377**, 790 (2006).

[31] *Quantum Theory of Angular Momentum*, D. A. Varshalovich, A. N. Moskalev, and V. K. Khersonskii (World Scientific, Singapore, 1988).

[32] V. G. Grachev, Sov. Phys. JETP **65**, 1029 (1987).

[33] H. A. Buckmaster, R. Chaterjee, and Y. H. Shing, Phys. Stat. Sol. (a) **13**, 9 (1972).

[34] C. Rudowicz, Magn. Reson. Rev. **13**, 1 (1987).

[35] M. L. Meilman and M. I. Samoilovich, *Introduction to EPR Spectroscopy of Activated Monocrystals* (Atomizdat, Moscow, 1977) (in Russian).

[36] A. Schweiger and G. Jeschke, *Principles of Pulse Electron Paramagnetic Resonance* (Oxford University Press, Oxford, 2001).

[37] E. Baibekov, JETP Lett. **93**, 292 (2011).

[38] R. Boscaino, F. M. Gelardi, and J. P. Korb, Phys. Rev. B **48**, 7077 (1993).

[39] R. N. Shakhmuratov, F. M. Gelardi, and M. Cannas, Phys. Rev. Lett. **79**, 2963 (1997).

[40] E. Malguth, A. Hoffmann, and M. R. Phillips, Phys. Stat. Sol. (b) **245**, 455 (2008).

[41] A. S. Gurin, N. G. Romanov, D. O. Tolmachev, P. G. Baranov, and C. Morhain, J Phys: Conf. Ser. **461**, 012032 (2013).

[42] A. Abragam and H. M. L. Pryce, Proc. Roy. Soc. (London) A **205**, 135 (1951).

[43] A. Abragam and B. Bleaney, *Electron Paramagnetic Resonance of Transition Ions* (Clarendon, Oxford, 1970).

[44] B. Bleaney, Proc. Phys. Soc. **73**, 939 (1959).

[45] G. F. Koster and H. Statz, Phys. Rev. **113**, 445 (1959).

[46] G. F. Koster, J. O. Dimmock, R. G. Wheeler, and H. Statz, *Properties of the Thirty-Two Point Groups* (MIT, Cambridge, 1963).

[47] F. S. Ham, in *Electron Paramagnetic Resonance*, edited by S. Geschwind (Plenum, New York, 1972).

[48] M. D. Sturge, in *Solid State Physics 20*, edited by F. Seitz and D. Turnbull (Academic, New York, 1967).